

# Amantadine-induced conformational and dynamical changes of the influenza M2 transmembrane proton channel

Sarah D. Cady and Mei Hong<sup>†</sup>

Department of Chemistry, Iowa State University, Ames, IA 50011

Communicated by William F. DeGrado, University of Pennsylvania School of Medicine, Philadelphia, PA, December 12, 2007 (received for review August 8, 2007)

**The M2 protein of influenza A virus forms a transmembrane proton channel important for viral infection and replication. Amantadine blocks this channel, thus inhibiting viral replication. Elucidating the high-resolution structure of the M2 protein and its change upon amantadine binding is crucial for designing antiviral drugs to combat the growing resistance of influenza A viruses against amantadine. We used magic-angle-spinning solid-state NMR to determine the conformation and dynamics of the transmembrane domain of the protein M2TMP in the apo- and amantadine-bound states in lipid bilayers. <sup>13</sup>C chemical shifts and torsion angles of the protein in 1,2-dilauroyl-*sn*-glycero-3-phosphatidylcholine (DLPC) bilayers indicate that M2TMP is  $\alpha$ -helical in both states, but the average conformation differs subtly, especially at the G34–I35 linkage and V27 side chain. In the liquid-crystalline membrane, the complexed M2TMP shows dramatically narrower lines than the apo peptide. Analysis of the homogeneous and inhomogeneous line widths indicates that the apo-M2TMP undergoes significant microsecond-time scale motion, and amantadine binding alters the motional rates, causing line-narrowing. Amantadine also reduces the conformational heterogeneity of specific residues, including the G34/I35 pair and several side chains. Finally, amantadine causes the helical segment N-terminal to G34 to increase its tilt angle by 3°, and the G34–I35 torsion angles cause a kink of 5° in the amantadine-bound helix. These data indicate that amantadine affects the M2 proton channel mainly by changing the distribution and exchange rates among multiple low-energy conformations and only subtly alters the average conformation and orientation. Amantadine-resistant mutations thus may arise from binding-incompetent changes in the conformational equilibrium.**

high-resolution structure | membrane protein | solid-state NMR | conformational heterogeneity | chemical-shift perturbation

**T**he M2 protein of the influenza A virus forms a membrane-bound proton channel that acidifies the endosomally trapped virus, which triggers the release of the viral RNA into the infected cell, initiating viral replication (1, 2). The cationic amine amantadine inhibits viral replication by blocking this proton channel and thus has been used for the prophylaxis and treatment of influenza A infections (3, 4). However, in the last few years, amantadine resistance has skyrocketed among influenza A viruses in Asia and North America (5), making it imperative to develop alternative antiviral drugs.

The M2 protein contains a transmembrane  $\alpha$ -helical domain (6) that has the essential amantadine-sensitive proton channel activity of the intact protein (7). Mutagenesis and electrophysiological experiments showed that the residues important for proton conduction and amantadine interaction lie on one face of the helix, namely, V27, A30, S31, and G34 (8, 9). Neutron diffraction data indicated that the amantadine ring is localized at  $\approx 6$  Å from the center of dioleoylphosphatidylcholine (DOPC) bilayers, close to V27 (10). Fourier analysis of the periodic oscillations in the channel reversal potential, pH-sensitive current, and amantadine resistance of cysteine mutants of the M2

protein yielded a functional structure of the channel (11). The active form of the channel is a tetramer for the intact protein (12, 13) and the transmembrane peptide (M2TMP) (14), as shown by <sup>19</sup>F solid-state NMR (SSNMR) of the membrane-bound peptide.

The most extensive molecular-level structural information of M2TMP came from static <sup>15</sup>N SSNMR data of Cross and coworkers (15, 16). Using uniaxially aligned lipid membranes, they determined the orientation of M2TMP in the apo (15) and complexed (16) states from <sup>15</sup>N chemical shift and N–H dipolar couplings. The apo peptide is tilted by 38° from the bilayer normal (15), whereas the amantadine-complexed peptide exhibits a kink with 31° and 20° tilt angles (16). However, sample preparation conditions such as solvents, membrane composition, and peptide concentration varied greatly in these studies, which may contribute to the observed orientation difference. From the <sup>15</sup>N orientational data, no direct information on the backbone and side chain conformations can be extracted. The side chain conformation may be especially sensitive to amantadine binding, yet so far only one <sup>13</sup>C–<sup>15</sup>N distance (17) and four <sup>19</sup>F–<sup>19</sup>F distances (14, 18) have been reported. Recently, amantadine was found to cause substantial narrowing of the <sup>15</sup>N NMR spectra (19, 20), suggesting that it either reduces the conformational heterogeneity or changes the dynamics of the protein, but which factor dominates is unknown.

To elucidate the atomic-resolution conformation and dynamics of the backbone and side chains of this important proton channel with and without amantadine, we have used magic-angle-spinning (MAS) <sup>13</sup>C and <sup>15</sup>N NMR techniques on M2TMP bound to 1,2-dilauroyl-*sn*-glycero-3-phosphatidylcholine (DLPC) bilayers. To identify sites of structural perturbation, we measured and compared the <sup>13</sup>C and <sup>15</sup>N isotropic shifts and torsion angles of eight residues spread throughout the peptide. The data indicate that amantadine most significantly perturbs the backbone of G34 and I35 and the side chain of V27. Analysis of the homogeneous and inhomogeneous <sup>13</sup>C line widths in the gel and liquid-crystalline (LC) phases of the membrane indicates that the apo peptide backbone undergoes significant motion on the microsecond time scale. Amantadine binding alters the motional rates and reduces the conformational distribution. Thus, the central feature of M2TMP structure appears to be the presence of multiple low-energy conformations, which are readily modified and selected by amantadine.

## Results and Discussion

**M2TMP Conformation With and Without Amantadine.** We chose eight residues in M2TMP for <sup>13</sup>C- and <sup>15</sup>N-labeling. Based on the

Author contributions: M.H. designed research; S.D.C. performed research; S.D.C. and M.H. analyzed data; and M.H. wrote the paper.

The authors declare no conflict of interest.

<sup>†</sup>To whom correspondence should be addressed. E-mail: mhong@iastate.edu.

This article contains supporting information online at [www.pnas.org/cgi/content/full/0711500105/DC1](http://www.pnas.org/cgi/content/full/0711500105/DC1).

© 2008 by The National Academy of Sciences of the USA

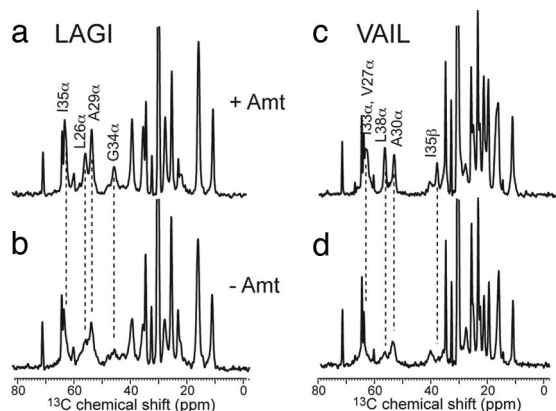


**Fig. 1.**  $^{13}\text{C}$  CP-MAS spectra of M2TMP at 303 K with (a and c) and without (b and d) amantadine. (a and b) LAGI. (c and d) VAIL. Note the significant line-narrowing and intensity increase in the presence of amantadine.

approximate seven-residue periodicity of the protein (11), these sites cover channel-lining positions (V27, A30, and G34), helix-helix interfaces (L26, I33, and L38), and lipid-facing positions (A29 and I35). In this way, we assess the impact of amantadine binding to M2TMP structure from all regions of the tetrameric bundle. Two peptides were synthesized that each contained four uniformly  $^{13}\text{C}$ ,  $^{15}\text{N}$ -labeled residues. The “LAGI” sample contained labeled L26, A29, G34, and I35, and the “VAIL” sample contained labeled V27, A30, I33, and L38. Fig. 1 shows representative  $^{13}\text{C}$  cross-polarization (CP) MAS spectra of the peptide in DLPC bilayers with (red) and without (black) amantadine at 303 K. The  $^{13}\text{C}$  isotropic line widths narrow substantially upon amantadine binding. In the apo peptide, many backbone signals such as G34  $\text{C}^\alpha$  are broad and poorly defined, whereas with amantadine, all  $\text{C}^\alpha$  resonances narrow and increase in intensity. Side chain signals also are narrowed but less dramatically. This  $^{13}\text{C}$  line-narrowing is similar to that seen in  $^{15}\text{N}$  spectra of the protein (16, 19). In the next section, we investigate the origin of this line-narrowing.

To determine the M2TMP conformation and its perturbation by amantadine, we measured the  $^{13}\text{C}$  and  $^{15}\text{N}$  isotropic chemical shifts of the peptide without and with amantadine.  $^{13}\text{C}$ — $^{13}\text{C}$  2D double-quantum (DQ)-filtered correlation spectra and  $^{15}\text{N}$ — $^{13}\text{C}$  correlation spectra were measured at 243 K where the peptide motion is frozen. Both spectra remove all lipid natural-abundance  $^{13}\text{C}$  signals, thus simplifying resonance assignment. Fig. 2 shows the 2D  $^{13}\text{C}$ — $^{13}\text{C}$  correlation spectra of LAGI and VAIL with (red) and without (black) amantadine. The spectra are readily assigned based on the connectivity patterns. Various chemical-shift changes are observed, for example, at V27 $\alpha$ , A30 $\beta$ , I35 $\gamma$ 1, and L38 $\beta$ . The largest  $\text{C}^\alpha$  shift change occurs at V27, which exhibits a 1.0-ppm upfield shift in the complex. G34  $\text{C}^\alpha$  is not detected in the 2D  $^{13}\text{C}$ — $^{13}\text{C}$  correlation spectrum because of the DQ excitation condition, but its signal is visible in the 2D  $^{15}\text{N}$ — $^{13}\text{C}$  spectra [supporting information (SI) Fig. 7] and shows a downfield  $^{15}\text{N}$  chemical-shift change of 2.5 ppm. Interestingly, the two Ile residues flanking G34 also exhibit  $^{15}\text{N}$  chemical-shift changes but in opposite directions, causing their amantadine-bound  $^{15}\text{N}$  shifts to differ by 5.8 ppm. SI Table 2 lists the isotropic shifts of the apo and complexed M2TMP.

Despite the chemical-shift perturbations by amantadine, no change is large enough to indicate a nonhelical structure (21), which is reflected by the positive  $\text{C}^\alpha$  and  $\text{C}'$  secondary shifts and negative  $\text{C}^\beta$  secondary shifts (Fig. 3 a–c) for all eight labeled residues. Fig. 3d plots the amantadine-induced average absolute chemical-shift changes of each residue. The maximum perturbation occurs at the channel-lining G34, followed by its adjacent

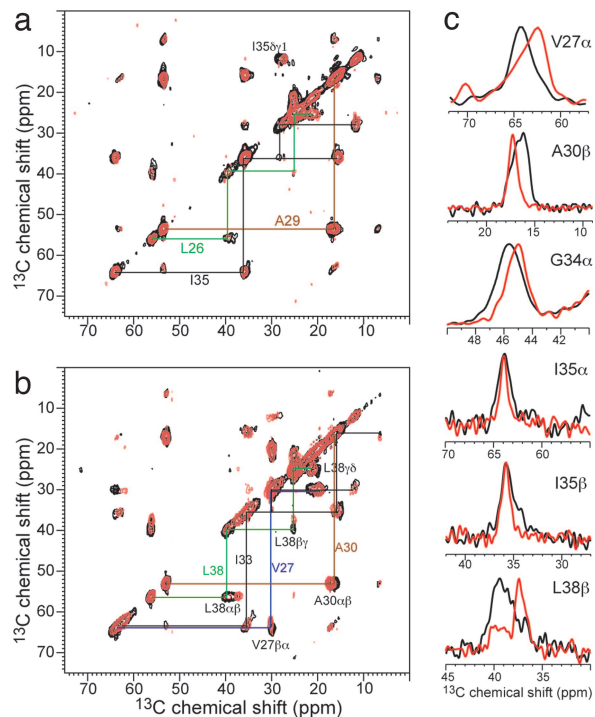


**Fig. 2.** 2D  $^{13}\text{C}$ — $^{13}\text{C}$  DQ-filtered spectra of M2TMP in DLPC bilayers without (black) and with (red) amantadine at 243 K. Intraresidue connectivities and cross-peaks with chemical-shift changes are indicated. (a) LAGI. (b) VAIL. (c) Selected 1D cross-sections that exhibit line-narrowing and chemical-shift changes upon amantadine binding. The G34 $\alpha$  trace was extracted from 1D CP spectra.

I35 and I33. A second local maximum is seen at V27, consistent with its proximity to amantadine (10). In terms of residue location, the channel-lining residues, the interfacial residues, and the lipid-facing residues except for the G34-neighboring I35 have

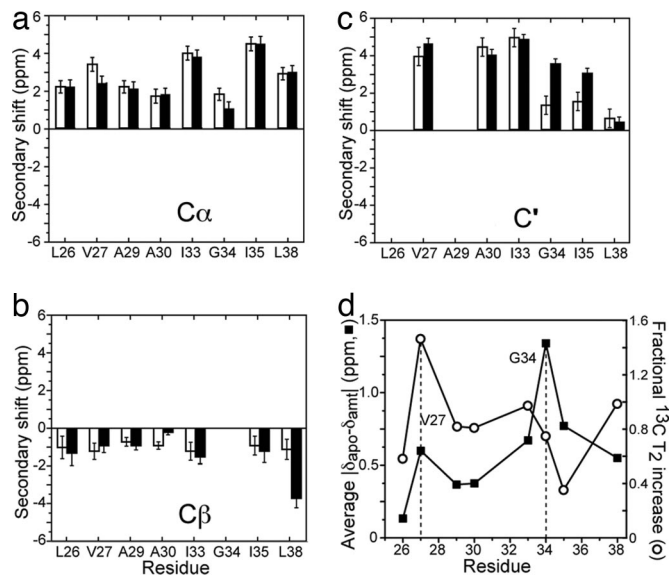


**Fig. 3.** Amantadine-induced isotropic shift and  $T_2$  changes of M2TMP. (a–c) Secondary shifts are plotted for  $\text{C}^\alpha$  (a),  $\text{C}^\beta$  (b), and  $\text{C}'$  (c). Open and filled bars correspond to the apo and complexed M2TMP, respectively. The average chemical-shift uncertainty is 0.35 ppm, estimated from the intrinsic line widths of the spectra. (d) Average absolute chemical-shift changes (filled squares) and fractional  $^{13}\text{C}$   $T_2$  increase at 303 K (open circles). Local maxima of chemical shift and  $T_2$  perturbation occur at V27 and G34.



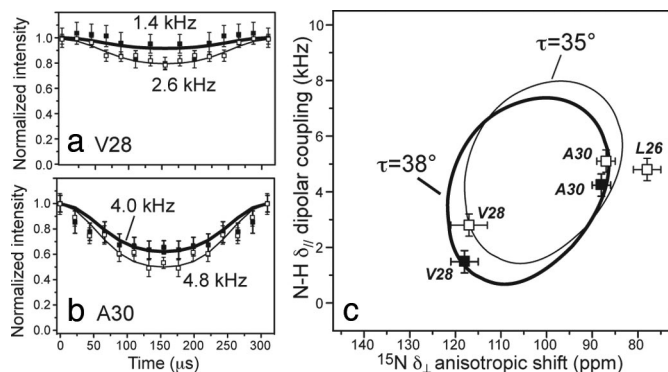


**Fig. 5.** Orientation of amantadine-bound M2TMP. (a and b)  $^{15}\text{N}$ – $^1\text{H}$  dipolar coupling of unoriented M2TMP in DLPC bilayers with amantadine (filled squares, thick line). For comparison, the apo peptide data published recently are superimposed (open squares, thin line) (31). (a) V28. (b) A30. (c) PISA wheels of M2TMP constructed from the  $\delta_{\parallel}$  N–H dipolar couplings and  $\delta_{\perp}$   $^{15}\text{N}$  anisotropic shifts. The data fit to a wheel with a tilt angle  $\tau$  of  $38^\circ$  (thick line). The apo peptide shows a  $\tau = 35^\circ$  (open symbols, thin line) (31).

temperature-dependent  $T_2$  curves, consistent with their motion being facilitated by a widening of the pore.

To assess the conformational heterogeneity of the protein, we compare the homogeneous line widths  $\Delta$  derived from the  $T_2$  with the apparent line widths  $\Delta^*$  measured from the spectra. In the LC phase, the  $\text{C}^\alpha$  line width of apo-M2TMP is almost completely homogeneously broadened by motion, as seen by the similar  $\Delta$  and  $\Delta^*$  (SI Fig. 9). Amantadine binding reduces  $\Delta$  by a factor of two. For the side chains, conformational heterogeneity is detectable in both the apo and complexed peptide because of narrower intrinsic line widths. To evaluate the conformational heterogeneity without different homogeneous line widths between the apo and complexed peptide, we froze the DLPC-bound M2TMP to 243 K, where the homogeneous line widths become similar between the two states (SI Table 5). Under this condition, most sites show similar  $\Delta^*$  and hence similar conformational heterogeneity between the apo and complexed peptide. The exceptions are G34, I35, and the side chains of L26, A30, and L38, where the complexed peptide has significantly narrower lines, indicating reduced conformational heterogeneity; this also is seen in the cross-sections of the  $^{13}\text{C}$  2D spectra (Fig. 2c).

In summary, in the LC phase of the lipid bilayer, the apo-M2TMP backbone undergoes large-amplitude microsecond-time scale motion that causes significant homogeneous broadening of the  $^{13}\text{C}$  spectra and consequent loss of intensity. Amantadine binding increases the  $T_2$  relaxation times for all sites by changing the motional rates, thus narrowing the intrinsic line widths. When the motion is frozen, the conformational distribution of the peptide is revealed to be reduced by amantadine at specific residues, including the G34–I35 junction and several methyl-rich side chains.

**Amantadine-Induced M2TMP Orientation Change.** We recently measured the orientation of the apo-M2TMP by using a powder-sample approach that exploits fast rigid-body uniaxial diffusion of the peptide backbone around the bilayer normal (31). Under this condition, motionally averaged powder spectra are obtained that indicate the peptide orientation from the bilayer normal (32). We now use this approach to determine the orientation of M2TMP in complex with amantadine.  $^{15}\text{N}$ – $^1\text{H}$  dipolar couplings and  $^{15}\text{N}$  chemical-shift anisotropies (CSA), which are extremely sensitive to the helix orientation, were measured. Fig. 5 a and b shows the N–H dipolar-shift (DIPSHIFT) curves of V28 and A30 at 313 K where the peptide is uniaxially mobile.

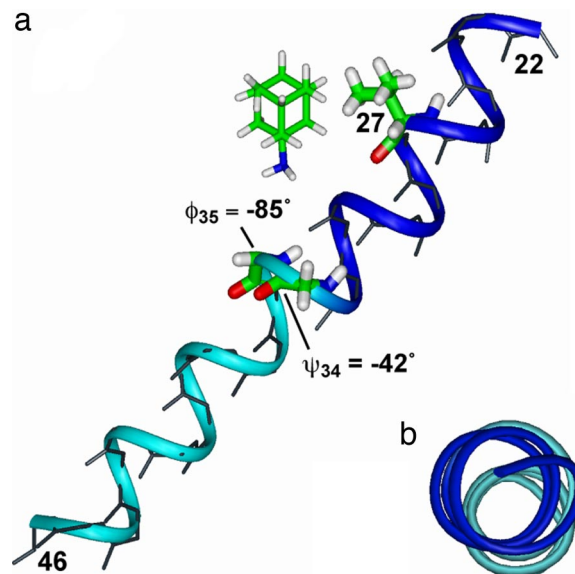


**Fig. 6.** Chemical shift and torsion-angle restrained backbone and partial side chain structure of amantadine-bound M2TMP. (a) Side view. (b) Top view. The exact position and orientation of amantadine is unknown and is shown here only as a reference to the peptide. The G34  $\psi$  and I35  $\phi$  angles create a helix kink of  $5^\circ$ , highlighted by the blue N-terminal and the cyan C-terminal segments.

Amantadine binding decreases the N–H dipolar coupling of both residues. Correlating the motionally averaged  $\delta_{\parallel}$  N–H dipolar coupling with the  $\delta_{\perp}$  edge of the  $^{15}\text{N}$  CSA obtained from static 1D spectra (data not shown), we obtain 2D “PISA wheels” (33, 34) (Fig. 5c). For the apo peptide in DLPC bilayers, previous data yielded a tilt angle  $\tau$  of  $35^\circ$  (31), whereas the current amantadine-bound M2TMP has a slightly larger  $\tau$  of  $38^\circ$ . The rotation angle of the wheel is unchanged. The  $3^\circ$  increase, although small, is consistent with amantadine binding at the N terminus of the helix, pushing it open slightly. The orientation of the segment C-terminal to G34 is not probed here because no  $^{15}\text{N}$  labels are used in that region.

Fig. 6 shows the chemical shift and torsion-angle constrained structure of M2TMP in the presence of amantadine, refined from the  $^{15}\text{N}$  NMR-derived model 1NYJ (15). At the G34–I35 junction, a G34  $\psi$  angle of  $-42^\circ$  and I35  $\phi$  of  $-85^\circ$  were used. The resulting helix shows a small kink of  $5^\circ$  between the segments N-terminal and C-terminal to G34, visible in the top view (Fig. 6b). The kink is defined as the angle between the average N–H bond orientation for residues 27–33 and for residues 37–43. This kink is reminiscent of the recent  $^{15}\text{N}$  NMR data of dimyristoylphosphatidylcholine (DMPC)-bound M2TMP, which showed a bend of  $11^\circ$  at G34 (16). We found that the exact value of the kink is sensitive to the G34/I35 torsion angles. With  $\psi_{34} = -60^\circ$ , the kink increases to  $\approx 16^\circ$ , whereas with a more ideal  $\phi_{35}$  of  $-60^\circ$ , the kink is almost completely removed.

## Conclusion

The NMR data here provide an extensive set of high-resolution conformational and dynamical constraints of the backbone and side chains of M2TMP in lipid bilayers without and with amantadine and elucidate the nature of the spectral line-narrowing caused by amantadine. The data indicate that amantadine binding to M2TMP exerts the largest effect on the dynamics and conformational heterogeneity of the protein, affects to a lesser extent the average backbone and side chain conformations, and only subtly affects the helix orientation. The apo peptide exhibits large-amplitude microsecond-time scale

motion that homogeneously broadens the NMR lines. Amantadine increases the motional rates of most backbone  $C^\alpha$  sites, causing substantial line-narrowing. It also reduces the conformational heterogeneity of certain residues, including G34, I35, and the side chains of L26, A30, and L38. Perturbation of the average conformation occurs mainly at G34–I35 and at the V27 side chain. Combined, the data strongly suggest that conformational plasticity is essential to proton conduction and gating of the apo channel, and at least part of amantadine's mechanism of action is to modify and select among the multiple low-energy conformations of M2TMP. This finding is consistent with energy surface mapping (35) and analytical ultracentrifugation data of M2TMP and its mutants (36, 37). It is possible, then, that amantadine resistance can arise from mutations that alter the protein conformational distribution and dynamics, thus preventing amantadine binding.

The observed large V27 chemical-shift and  $T_2$  changes are in excellent agreement with mutagenesis data indicating strong interaction of this residue with amantadine. Mutation of V27 to Ala, Ser, Ile, and Thr caused either complete or partial resistance to amantadine in various viral strains (3, 9). Thus, the interaction of amantadine with the channel is exquisitely sensitive to the size and hydrophobicity of the side chain at this position.

Complexed with amantadine, the M2TMP helix shows a small degree of nonideality in the backbone torsion angles. In particular, the deviation of the G34–I35 conformation from the ideal helix geometry causes a helix kink of  $5^\circ$ , which may have an effect on the interhelical interaction of H37 imidazole rings downstream (19). The exact value of the kink and the exact orientation of the helix in the DLPC membrane differ slightly from those found in the DMPC membrane. Given the differences in sample preparation conditions, such as membrane thickness and the state of alignment (19, 20), these differences further underscore the structural plasticity of the peptide. The spectra of the amantadine-bound M2TMP show a single signal for each label; thus, the four helices of the tetramer are rotationally symmetric and chemically identical. This conclusion implies that, in the LC phase, not only does amantadine have the same uniaxial mobility as the tetrameric bundle, but it also exchanges among the four helices on a time scale faster than the nuclear spin interactions ( $<10^{-5}$  s) (19).

## Materials and Methods

**Peptides and Lipids.** Fmoc-protected uniformly  $^{13}\text{C}$ ,  $^{15}\text{N}$ -labeled amino acids were either prepared in-house (38) or purchased from Sigma and Cambridge Isotope Laboratories. The transmembrane peptide of the M2 protein of the Udorn strain (residues 22–46) (39) was synthesized by PrimmBiotech (Cambridge, MA) and purified to  $>95\%$  purity. The amino acid sequence is SSD-PLVVAASIIILHLILWLDRL. In addition to peptides containing multiple uniformly  $^{13}\text{C}$ ,  $^{15}\text{N}$ -labeled residues, two peptides each containing a single  $^{15}\text{N}$  label at V28 and A30 were synthesized for orientation measurements.

**Membrane Sample Preparation.** M2TMP was reconstituted into lipid vesicles by detergent dialysis (18). DLPC lipids were chosen because of the favorable dynamics of the protein in this membrane (31) and the similar phase transition temperature ( $-2^\circ\text{C}$ ) of this bilayer to biological membranes. The vesicle solution was prepared by suspending dry DLPC powder (Avanti Polar Lipids) in 1 ml of phosphate buffer (10 mM  $\text{Na}_2\text{HPO}_4/\text{NaH}_2\text{PO}_4$ , 1 mM EDTA, and 0.1 mM  $\text{NaN}_3$ ) at pH 7.5, vortexing and freeze-thawing six to eight times to create uniform vesicles of  $\approx 200\text{-nm}$  diameter (40). M2TMP powder was codissolved with the detergent octyl- $\beta$ -D-glucopyranoside (OG) in 2 ml of phosphate

buffer to reach an OG concentration of 30 mg/ml. The M2TMP/OG solution then was mixed with the DLPC vesicle solution, giving a final OG concentration of 15 mg/ml. The mixture was vortexed for 1 h, allowed to stand for 6–8 h at room temperature, and then dialyzed with a 3.5-kDa cutoff against 1 liter of phosphate buffer at  $4^\circ\text{C}$  for 3 days with buffer changes every 8–12 h to ensure complete removal of the detergent. The dialyzed M2TMP/DLPC solution was centrifuged at  $150,000 \times g$  for 3 h at  $10^\circ\text{C}$  to give a wet pellet with  $\approx 50\text{ wt } \%$  water. The final peptide/lipid (P/L) molar ratio is 1:15. UV-visible spectrum of the supernatant indicated  $\approx 98\%$  binding of the peptide to the membrane. For amantadine-bound samples, 10 mM amantadine hydrochloride was added to the phosphate buffer throughout the lipid vesicle formation and peptide assembly process.

For orientation measurements,  $^{15}\text{N}$ -labeled M2TMP was codissolved with DLPC lipids in trifluoroethanol at a P/L of 1:20, lyophilized, and then rehydrated to 50 wt % water with a pH 8.1 phosphate buffer. For amantadine-bound samples, 2 mmol of amantadine hydrochloride was added to the dry M2TMP/lipid mixture before dissolution in trifluoroethanol.

**SSNMR Spectroscopy.** Most NMR experiments were carried out on a Bruker (Karlsruhe, Germany) AVANCE-600 (14.1-T) spectrometer by using a 4-mm triple-resonance MAS probe.  $^{13}\text{C}$ – $^{13}\text{C}$  and  $^{15}\text{N}$ – $^{13}\text{C}$  2D correlation and torsion angle experiments were conducted at 243 K to freeze peptide motion. All other parameters, including  $^{15}\text{N}$  CSA,  $^{15}\text{N}$ – $^1\text{H}$  dipolar coupling, and  $^{13}\text{C}$   $T_2$  relaxation times, were measured at 303 K or 313 K where the peptide is uniaxially mobile in the LC phase of the DLPC bilayer. Typical radiofrequency pulse lengths were 5  $\mu\text{s}$  for  $^{13}\text{C}$  and 3.5–4.0  $\mu\text{s}$  for  $^1\text{H}$ .  $^1\text{H}$  TPPM (41) or SPINAL (42) decoupling of 60–70 kHz were applied.  $^{13}\text{C}$  chemical shifts were referenced to the  $\alpha$ -Gly C' signal at 176.49 ppm on the TMS scale, and  $^{15}\text{N}$  chemical shifts were referenced to the  $^{15}\text{N}$  signal of *N*-acetyl-valine at 122 ppm on the liquid ammonia scale. For G34 torsion angles extraction from TALOS, the  $^{13}\text{C}$  chemical shifts were converted to the 3-(trimethylsilyl)-propionate scale by adding 1.82 ppm to the measured shifts.

2D DQ-filtered  $^{13}\text{C}$ – $^{13}\text{C}$  correlation spectra were measured by using a SPCS sequence (43)  $<7\text{-kHz}$  MAS. DQ filtration removes lipid background  $^{13}\text{C}$  signals, thus simplifying assignment of the protein signals. 2D  $^{15}\text{N}$ – $^{13}\text{C}$  correlation spectra were measured by using a REDOR pulse train (44) of 0.7–2.1 ms for  $^{13}\text{C}$ – $^{15}\text{N}$  coherence transfer (45).

$\phi$  angles were measured under 6.5-kHz MAS by using the HNCH technique, with doubling of the N–H dipolar coupling to enhance the angular resolution (22, 46).  $^1\text{H}$ – $^1\text{H}$  homonuclear coupling was removed by an FSLG sequence (47). The HNCH data were simulated by using a doubled N–H coupling of 12.0 kHz and a C–H dipolar coupling of 12.5 kHz, both scaled by the FSLG scaling factor of 0.577. These values were directly measured by C–H and N–H DIPSHIFT correlation experiments on the protein at 243 K.  $\psi$  angle was measured with the NCCN experiment (23) correlating the  $\text{N}_i$ – $\text{C}^\alpha_i$  and  $\text{C}'_i$ – $\text{N}_{i+1}$  bond orientations. Spinning speeds of 4 and 5 kHz were used to obtain multiple time points on the angle-dependent curve.  $\chi_{\text{H}}$  torsion angles ( $\text{H}^\alpha$ – $\text{C}^\alpha$ – $\text{C}^\beta$ – $\text{H}^\beta$ ) were measured by correlating the  $\text{C}^\alpha$ – $\text{H}^\alpha$  and  $\text{C}^\beta$ – $\text{H}^\beta$  bond orientations by using a modified HCCH technique (25) under 9-kHz MAS. A HORROR sequence with a resonance condition of  $\omega_1 = \omega/2$  (48) was used to selectively excite the  $\text{C}^\alpha$ – $\text{C}^\beta$  DQ coherence, followed by a dipolar-doubled C–H DIPSHIFT period. A doubled and FSLG-scaled C–H dipolar coupling of 26.0 kHz was used to simulate the angle-dependent curves. All these torsion angles have an inherent double degeneracy caused by the uniaxial nature of the dipolar coupling. The wrong angle is readily identified by the fact that it falls into either unpopulated regions of the Ramachandran diagram or the  $\beta$ -sheet region, which contradicts NMR chemical shifts.

$^{15}\text{N}$ – $^1\text{H}$  dipolar couplings for orientation determination were obtained from a dipolar-doubled DIPSHIFT experiment (46, 49, 50) under 7-kHz MAS. An FSLG sequence with an effective field of 76.5 kHz was used for  $^1\text{H}$  homonuclear decoupling.

**ACKNOWLEDGMENTS.** We thank Prof. Yoshitaka Ishii for help with the TALOS simulation. This work is supported by National Science Foundation Grants MCB-0543473 and DBI-0421374.

- Pinto LH, Holsinger LJ, Lamb RA (1992) Influenza virus M2 protein has ion channel activity. *Cell* 69:517–528.
- Pinto LH, Lamb RA (2007) Controlling influenza virus replication by inhibiting its proton flow. *Mol Bio Syst* 3:18–23.
- Wang C, Takeuchi K, Pinto LH, Lamb RA (1993) Ion channel activity of influenza A virus M2 protein: characterization of the amantadine block. *J Virol* 67:5585–5594.
- Lamb RA, Holsinger KJ, Pinto LH (1994) in *Cellular Receptors of Animal Viruses*, ed Wemmer E (Cold Spring Harbor Lab Press, Plainview, NY), pp 303–321.
- Bright RA, et al. (2005) Incidence of adamantane resistance among influenza A (H3N2) viruses isolated worldwide from 1994 to 2005: A cause for concern. *Lancet* 366:1175–1181.
- Duff KC, Kelly SM, Price NC, Bradshaw JP (1992) The secondary structure of influenza A M2 transmembrane domain: A circular dichroism study. *FEBS Lett* 311:256–258.
- Duff KC, Ashley RH (1992) The transmembrane domain of influenza A M2 protein forms amantadine-sensitive proton channels in planar lipid bilayers. *Virology* 190:485–489.
- Hay AJ, Wolstenholme AJ, Skehel JJ, Smith MH (1985) The molecular basis of the specific anti-influenza action of amantadine. *EMBO J* 4:3021–3024.
- Holsinger LJ, Nichani D, Pinto LH, Lamb RA (1994) Influenza A virus M2 ion channel protein: A structure-function analysis. *J Virol* 68:1551–1563.
- Duff KC, Gilchrist PJ, Saxena AM, Bradshaw JP (1994) Neutron diffraction reveals the site of amantadine blockade in the influenza A M2 ion channel. *Virology* 202:287–293.

11. Pinto LH, et al. (1997) A functionally defined model for the M2 proton channel of influenza A virus suggests a mechanism for its ion selectivity. *Proc Natl Acad Sci USA* 94:11301–11306.
12. Sakaguchi T, Tu Q, Pinto LH, Lamb RA (1997) The active oligomeric state of the minimalistic influenza virus M2 ion channel is a tetramer. *Proc Natl Acad Sci USA* 94:5000–5005.
13. Salom D, Hill BR, Lear JD, DeGrado WF (2000) pH-dependent tetramerization and amantadine binding of the transmembrane helix of M2 from the influenza A virus. *Biochemistry* 39:14160–14170.
14. Luo W, Hong M (2006) Determination of the oligomeric number and intermolecular distances of membrane protein assemblies by anisotropic  $(1)H$ -driven spin diffusion NMR spectroscopy. *J Am Chem Soc* 128:7242–7251.
15. Wang J, Kim S, Kovacs F, Cross TA (2001) Structure of the transmembrane region of the M2 protein H (+) channel. *Protein Sci* 10:2241–2250.
16. Hu J, et al. (2007) Backbone structure of the amantadine-block trans-membrane domain M2 proton channel from influenza A virus. *Biophys J* 92:4335–4343.
17. Nishimura K, Kim S, Zhang L, Cross TA (2002) The closed state of a H<sup>+</sup> channel helical bundle combining precise orientational and distance restraints from solid state NMR. *Biochemistry* 41:13170–13177.
18. Luo W, Mani R, Hong M (2007) Side chain conformation and gating of the M2 transmembrane peptide proton channel of influenza A virus from solid-state NMR. *J Phys Chem* 111:10825–10832.
19. Hu J, Riqiang F, Cross TA (2007) The chemical and dynamical influence of the anti-viral drug amantadine on the M2 proton channel transmembrane domain. *Biophys J* 93:276–283.
20. Li C, Qin H, Gao FP, Cross TA (2007) Solid-state NMR characterization of conformational plasticity within the transmembrane domain of the influenza A M2 proton channel. *Biochim Biophys Acta* 1768:3162–3170.
21. Zhang H, Neal S, Wishart DS (2003) RefDB: A database of uniformly referenced protein chemical shifts. *J Biomol NMR* 25:173–195.
22. Hong M, Gross JD, Griffin RG (1997) Site-resolved determination of peptide torsion angle  $\phi$  from the relative orientations of backbone N—H and C—H bonds by solid-state NMR. *J Phys Chem B* 101:5869–5874.
23. Costa PR, Gross JD, Hong M, Griffin RG (1997) Solid-state NMR measurement of  $\psi$  in peptides: A NCCN 2Q-heteronuclear local field experiment. *Chem Phys Lett* 280:95–103.
24. Cornilescu G, Delaglio F, Bax A (1999) Protein backbone angle restraints from searching a database for chemical shift and sequence homology. *J Biomol NMR* 13:289–302.
25. Feng X, et al. (1996) Direct determination of a molecular torsional angle by solid-state NMR. *Chem Phys Lett* 257:314–320.
26. Rothwell WP, Waugh JS (1981) Transverse relaxation of dipolar coupled spin systems under RF irradiation: Detecting motions in solids. *J Chem Phys* 74:2721–2732.
27. Hahn EL (1950) Spin echoes. *Phys Rev* 80:580–594.
28. Lesage A, Bardet M, Emsley L (1999) Through-bond carbon–carbon connectivities in disordered solids by NMR. *J Am Chem Soc* 121:10987–10993.
29. Sansom MS, Kerr ID (1993) Influenza virus M2 protein: A molecular modelling study of the ion channel. *Protein Eng* 6:65–74.
30. Astrahan P, Kass I, Cooper MA, Arkin IT (2004) A novel method of resistance for influenza against a channel-blocking antiviral drug. *Proteins Struct Funct Bioinf* 55:251–257.
31. Cady SD, Goodman C, Tatko CD, DeGrado WF, Hong M (2007) Determining the orientation of uniaxially rotating membrane proteins using unoriented samples: A 2H, 13C, and 15N solid-state NMR investigation of the dynamics and orientation of a transmembrane helical bundle. *J Am Chem Soc* 129:5719–5729.
32. Hong M, Doherty T (2006) Orientation determination of membrane-disruptive proteins using powder samples and rotational diffusion: A simple solid-state NMR approach. *Chem Phys Lett* 432:296–300.
33. Marassi FM, Opella SJ (2000) A solid-state NMR index of helical membrane protein structure and topology. *J Magn Reson* 144:150–155.
34. Wang J, et al. (2000) Imaging membrane protein helical wheels. *J Magn Reson* 144:162–167.
35. Torres J, Kukol A, Arkin IT (2001) Mapping the energy surface of transmembrane helix–helix interactions. *Biophys J* 81:2681–2692.
36. Stouffer AL, Nanda V, Lear JD, DeGrado WF (2005) Sequence determinants of a transmembrane proton channel: An inverse relationship between stability and function. *J Mol Biol* 347:169–179.
37. Howard KP, Lear JD, DeGrado WF (2002) Sequence determinants of the energetics of folding of a transmembrane four-helix-bundle protein. *Proc Natl Acad Sci USA* 99:8568–8572.
38. Carpino LA, Han GY (1972) 9-Fluorenylmethoxycarbonyl amino-protecting group. *J Org Chem* 37:3404–3409.
39. Ito T, Gorman OT, Kawaoka Y, Bean WJ, Webster RG (1991) Evolutionary analysis of the influenza A virus M gene with comparison of the M1 and M2 proteins. *J Virol* 65:5491–5498.
40. Traikia M, Warschawski DE, Recouvreur M, Cartaud J, Devaux PF (2000) Formation of unilamellar vesicles by repetitive freeze-thaw cycles: Characterization by electron microscopy and 31P-nuclear magnetic resonance. *Eur Biophys J* 29:184–195.
41. Bennett AE, Rienstra CM, Auger M, Lakshmi KV, Griffin RG (1995) Heteronuclear decoupling in rotating solids. *J Chem Phys* 103:6951–6958.
42. Fung BM, Khitrik AK, Ermolaev K (2000) An improved broadband decoupling sequence for liquid crystals and solids. *J Magn Reson* 142:97–101.
43. Hohwy M, Rienstra CM, Jaroniec CP, Griffin RG (1999) Fivefold symmetric homonuclear dipolar recoupling in rotating solids: Application to double-quantum spectroscopy. *J Chem Phys* 110:7983–7992.
44. Gullion T, Schaefer J (1989) Rotational echo double resonance NMR. *J Magn Reson* 81:196–200.
45. Hong M, Griffin RG (1998) Resonance assignment for solid peptides by dipolar-mediated  $^{13}C/^{15}N$  correlation solid-state NMR. *J Am Chem Soc* 120:7113–7114.
46. Hong M, et al. (1997) Coupling amplification in 2D MAS NMR and its application to torsion angle determination in peptides. *J Magn Reson* 129:85–92.
47. Bielecki A, Kolbert AC, de Groot HJM, Griffin RG, Levitt MH (1990) Frequency-switched Lee-Goldburg sequences in solids. *Adv Magn Reson* 14:111–124.
48. Nielsen NC, Bildsoe H, Jakobsen HJ, Levitt MH (1994) Double-quantum homonuclear rotary resonance: Efficient dipolar recovery in magic-angle spinning nuclear magnetic resonance. *J Chem Phys* 101:1805–1812.
49. Huster D, Yamaguchi S, Hong M (2000) Efficient  $\beta$ -sheet identification in proteins by solid-state NMR spectroscopy. *J Am Chem Soc* 122:11320–11327.
50. Munowitz MG, Griffin RG, Bodenhausen G, Huang TH (1981) Two-dimensional rotational spin-echo nuclear magnetic resonance in solids: Correlation of chemical shift and dipolar interactions. *J Am Chem Soc* 103:2529–2533.

**Table 2.**  $^{13}\text{C}$  and  $^{15}\text{N}$  chemical shifts (ppm) of M2TMP in DLPC bilayers at 243 K without and with amantadine (Amt). Sites with chemical-shift differences greater than 0.5 ppm are bolded. The letters s, m, w denote strong, medium, and weak intensities when more than one peak is observed. The  $^{13}\text{C}$  and  $^{15}\text{N}$  shifts are referenced to TMS and liquid  $\text{NH}_3$ , respectively.

Residue	Site	- Amt	+ Amt
L26	N	117.7	117.5
	CO	-	-
	C $\alpha$	55.4	55.4
	C $\beta$	39.7	39.4
	C $\gamma$	25.2	25.1
	C $\delta$ 1	22.3	22.4
	C $\delta$ 2	21.2	21.3
	V27	N	120.4
CO		<b>177.9</b>	<b>178.6</b>
C $\alpha$		<b>63.8</b>	<b>62.8</b>
C $\beta$		29.8	30.1
C $\gamma$ 1		<b>21.0</b>	<b>20.0</b>
C $\gamma$ 2		19.5	19.9
A29	N	<b>120.9</b>	<b>121.7</b>
	CO	-	-
	C $\alpha$	53.3	53.2
	C $\beta$	16.7	16.5
A30	N	118.7	118.4
	CO	180.4	180.0
	C $\alpha$	52.8	52.9
	C $\beta$	<b>16.5</b>	<b>17.2</b>
I33	N	<b>120.2</b>	<b>118.8</b>
	CO	178.8	178.7
	C $\alpha$	63.3	63.1
	C $\beta$	35.7	35.5
	C $\gamma$ 1	<b>28.6</b>	<b>30.1</b>
	C $\gamma$ 2	<b>15.1</b>	<b>16.0</b>
	C $\delta$	11.8	12.2
G34	N	<b>107.1</b>	<b>106.3, 109.7</b>
	CO	<b>173.5</b>	<b>175.7</b>
	C $\alpha$	<b>45.6</b>	45.9, <b>44.8</b>
I35	N	<b>122.3</b>	<b>124.6</b>
	CO	<b>175.4</b>	<b>176.9</b>
	C $\alpha$	63.8	63.8

L38	C $\beta$	36.0	35.8
	C $\gamma$ 1	<b>28.2</b>	<b>27.0</b>
	C $\gamma$ 2	15.8	15.7
	C $\delta$	11.8	11.7
	N	<b>117.8</b>	<b>117.1</b>
	CO	175.8	175.6
	C $\alpha$	56.1	56.2
	C $\beta$	<b>39.6s, 36.8w</b>	39.7m, <b>37.0s</b>
	C $\gamma$	25.2	25.0
	C $\delta$ 1	<b>22.3</b>	<b>23.3</b>
	C $\delta$ 2	<b>20.1</b>	<b>21.2</b>

---

**Table 3.**  $^{13}\text{C}$  homogeneous  $T_2$  and apparent  $T_2^*$  (ms) of M2TMP in DLPC lipid bilayers without and with amantadine (Amt) at 303 K.  $T_2^*$  is obtained from the observed linewidths by  $T_2^* = 1/\pi\Delta^*$ .

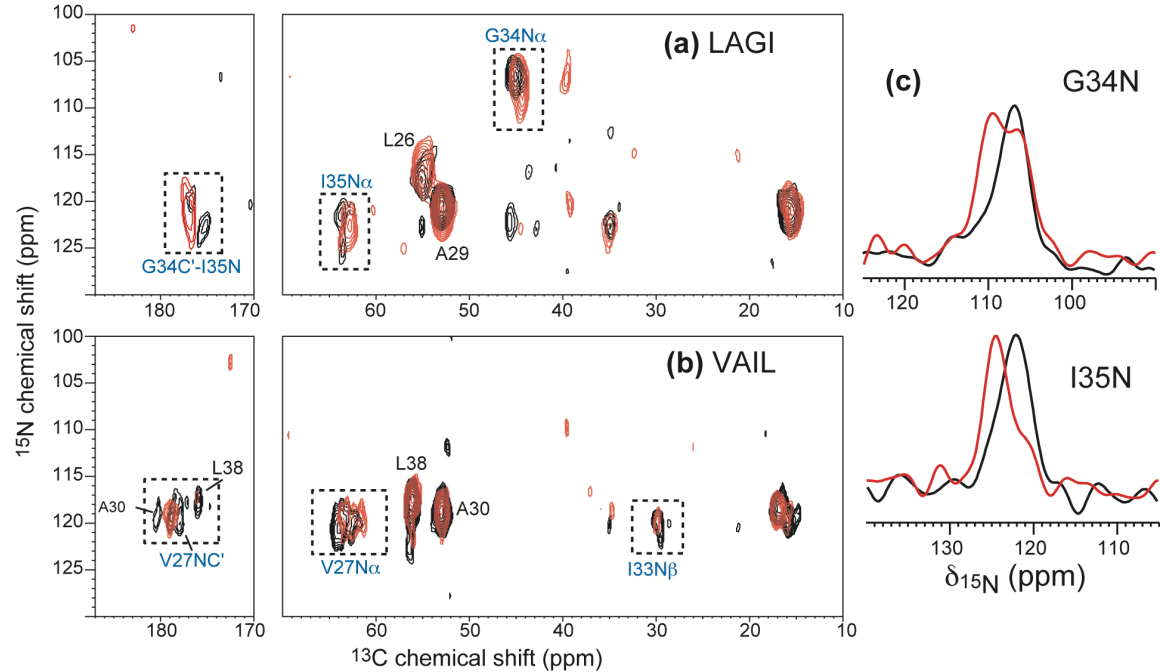
Residue	Site	$T_2^*$ , - Amt	$T_2$ , - Amt	$T_2^*$ , + Amt	$T_2$ , + Amt
L26	C $\alpha$	1.0	1.4	1.8	2.1
	C $\beta$	1.8	1.8	2.6	3.0
	C $\delta$ 1	3.2	5.8	4.7	9.2
	C $\delta$ 2	-	-	3.7	8.4
V27	C $\alpha$	1.1	1.0	1.3	3.4
	C $\gamma$ 2	3.7	4.7	3.4	7.2
A29	C $\alpha$	1.1	1.3	2.0	2.5
	C $\beta$	2.1	5.2	2.2	9.0
A30	C $\alpha$	1.1	1.8	2.1	3.5
	C $\beta$	2.2	3.4	1.3	5.7
I33	C $\alpha$	1.1	1.0	1.4	3.4
	C $\gamma$ 2	2.2	3.4	1.3	4.6
	C $\delta$	3.7	4.8	3.0	5.6
G34	C $\alpha$	0.9	1.2	1.3	2.1
I35	C $\alpha$	1.4	1.9	2.3	2.1
	C $\beta$	1.9	2.1	2.9	2.6
	C $\gamma$ 2	2.1	2.1	2.2	3.4
	C $\delta$	3.5	4.9	4.1	7.1
L38	C $\alpha$	1.2	1.3	2.1	3.5
	C $\beta$	1.2	1.5	2.3	3.6
	C $\gamma$	2.6	2.7	2.1	3.5
	C $\delta$ 1	3.3	4.5	3.8	8.3
	C $\delta$ 2	3.7	4.7	3.0	8.0
Average		2.1	2.8	2.5	4.9

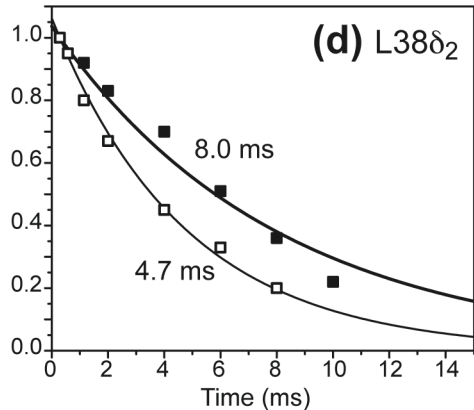
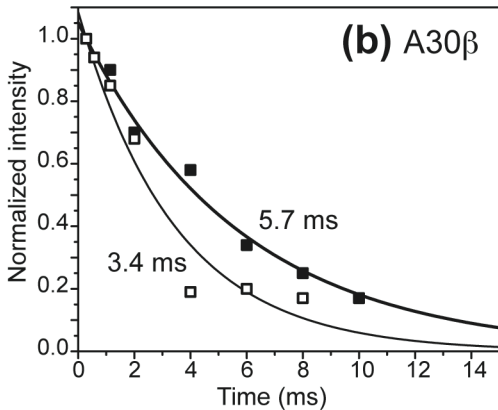
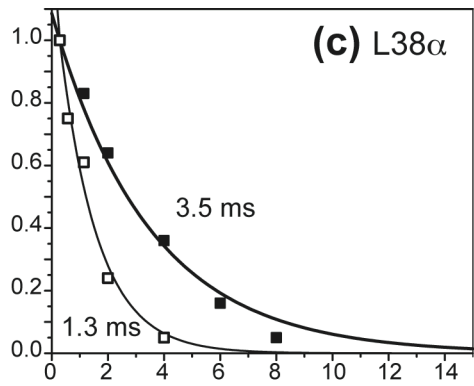
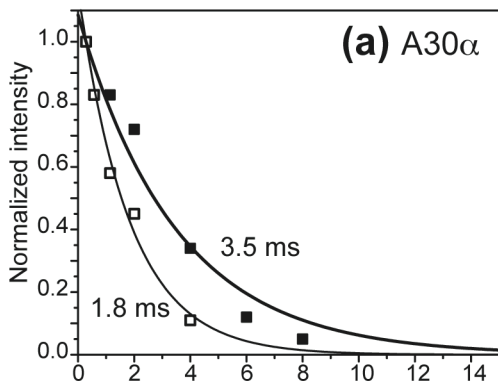
**Table 4.**  $^{13}\text{C}$  homogeneous  $T_2$  (ms) of M2TMP at 243 K and 303 K of M2TMP without and with amantadine (Amt).

Residue	Site	-Amt, 303 K	-Amt, 243 K	+Amt, 303 K	+Amt, 243 K
L26	C $\alpha$	1.4	3.0	2.1	2.8
	C $\beta$	1.8	1.8	3.0	1.5
	C $\gamma$		2.4		
	C $\delta$ 1	5.8	3.0	9.2	
	C $\delta$ 2			8.4	
V27	C $\alpha$	1.0	2.8	3.4	3.0
	C $\beta$		2.4		2.5
	C $\gamma$ 2	4.7	4.0	7.2	4.7
A29	C $\alpha$	1.3	3.2	2.5	2.8
	C $\beta$	5.2	4.6	9.0	4.9
A30	C $\alpha$	1.8	2.8	3.5	3.2
	C $\beta$	3.4	5.1	5.7	7.2
I33	C $\alpha$	1.0	2.8	3.4	3.0
	C $\beta$		2.3		2.8
	C $\gamma$ 1		2.4		2.5
	C $\gamma$ 2	3.4		4.6	
	C $\delta$	4.8	4.2	5.6	4.3
G34	C $\alpha$	1.2	3.2	2.1	2.6
I35	C $\alpha$	1.9	2.9	2.1	2.8
	C $\beta$	2.1	2.2	2.6	1.8
	C $\gamma$ 2	2.1		3.4	
	C $\delta$	4.9	5.3	7.1	4.7
L38	C $\alpha$	1.3	2.9	3.5	3.2
	C $\beta$	1.5	1.9	3.6	2.2
	C $\gamma$	2.7	2.7	3.5	3.0
	C $\delta$ 1	4.5	4.0	8.3	4.7
	C $\delta$ 2	4.7		8.0	

**Table 5.**  $^{13}\text{C}$  apparent line widths ( $\Delta^*$ ) and homogeneous line widths ( $\Delta$ ) (Hz) of M2TMP in DLPC bilayers at 243 K without and with amantadine (Amt). The apparent line widths  $\Delta^*$  ( $\pm 20$  Hz) are read off from 2D correlation spectra, while the homogeneous line widths  $\Delta$  are obtained from  $T_2$  measurements as  $\Delta = 1/\pi T_2$ . Sites of significant line width changes upon amantadine binding are bolded. Sites without entry are due to resonance overlap.

Residue	site	$\Delta^*$ , - Amt	$\Delta$ , - Amt	$\Delta^*$ , + Amt	$\Delta$ , + Amt
L26	C $\alpha$	170	100	200	110
	C $\beta$	<b>410</b>	180	<b>270</b>	200
V27	C $\alpha$	260	110	260	110
	C $\beta$	190	130	180	130
A29	C $\alpha$	160	100	140	110
	C $\beta$	240	70	240	70
A30	C $\alpha$	180	110	140	100
	C $\beta$	<b>310</b>	60	<b>160</b>	40
I33	C $\alpha$	300	110	300	110
	C $\beta$	260	140	230	110
	C $\gamma$ 1	360	130	370	130
	C $\gamma$ 2	310		280	
G34	C $\alpha$	<b>240</b>	100	<b>180</b>	120
I35	C $\alpha$	<b>250</b>	110	<b>130</b>	120
	C $\beta$	<b>240</b>	150	<b>160</b>	180
	C $\gamma$ 1	<b>290</b>		<b>170</b>	
	C $\gamma$ 2	210		210	
	C $\delta$	210	60	170	70
L38	C $\alpha$	190	100	150	100
	C $\beta$	<b>380</b>	160	<b>200</b>	150
Average		258	113	207	115





**- Amt**

**+ Amt**

**(a)**

**(c)**

289 Hz

backbone

177 Hz

227 Hz

114 Hz

**(b)**

**(d)**

120 Hz

sidechain

86 Hz

114 Hz

55 Hz

400 200 0 -200 -400

frequency (Hz)

400 200 0 -200 -400

frequency (Hz)

